Interfacial engineering for enhanced mechanical performance: High-entropy alloy/graphene nanocomposites

Yeran Shi [a], Wenting Ye [a], Dongpeng Hua [a], Qing Zhou [a,**], Zhuobin Huang [a], Yuxin Liu [b], Shuo Li [a], Ting Guo [b], Yongnan Chen [b], Stefan J. Eder [c,d,*], Haifeng Wang [a,***]

[a] State Key Laboratory of Solidification Processing, Center of Advanced Lubrication and Seal Materials, Northwestern Polytechnical University, Xi'an, Shaanxi, 710072, PR China
[b] School of Materials Science and Engineering, Chang'an University, Xi'an, 710064, China
[c] AC2T research GmbH, Viktor-Kaplan-Straße 2/C, Wiener Neustadt, 2700, Austria
[d] Institute for Engineering Design and Product Development, TU Wien, Lehárgasse 6 - Objekt 7, Vienna, 1060, Austria

ARTICLE INFO

ABSTRACT

In pursuit of high-performance materials, the synergistic combination of high-entropy alloys (HEAs) and graphene (Gr) has emerged as a promising approach. Here, we report a groundbreaking study on CoCrFeMnNi/Gr nanocomposites that highlights their exceptional mechanical properties. Leveraging on molecular dynamics simulations, we reveal the underlying mechanisms that govern the tensile behavior of these nanocomposites. Notably, we demonstrate that the introduction of graphene has a profound impact on the nucleation and propagation of dislocations in HEA. The interface between the HEA and graphene serves as a remarkable source for dislocations, leading to a transformative alteration of the dislocation behavior. Moreover, the high stresses accumulated at the interface drive graphene to undergo out-of-plane deformation, accommodating the plasticity of the HEA. We establish that the mechanical properties of these nanocomposites exhibit an intriguing dependence on the tensile direction and the thickness of HEA, which can be accurately described by a modified Hall-Petch relationship. Our findings provide crucial insights into the role of graphene in strengthening CoCrFeMnNi HEA/Gr composites, paving the way for the design of advanced materials with unprecedented strength and ductility. The extraordinary mechanical performance of HEA/Gr nanocomposites unravels a new frontier in materials science, with wide-ranging implications for a broad spectrum of applications, from aerospace to automotive and beyond.

1. Introduction

In recent years, high entropy alloys (HEA) have exhibited tremendous potential in the application of key fields such as navigation, aerospace, and nuclear energy, etc., in light of its excellent general performance [1–7]. The archetypal CoCrFeMnNi HEAs [8] have impressive properties in terms of fracture toughness [9], corrosion resistance [10], and ductility [11,12]. However, their insufficient strength due to the single-phase FCC crystal structure remains to be improved [13,14]. Although tremendous efforts have been devoted to strengthening strategies by grain refinement [15] or nitriding [16,17] and boronizing [18], the improvement of the mechanical properties is sometimes unsatisfactory.

Graphene [19], as one of the most eminent materials in the field of science and technology [20,21], has been used as a reinforcing phase in metallic materials to achieve superior mechanical properties [22] owing to its excellent strength and structural rigidity [23]. The introduction of graphene constitutes the introduction of 2D layered interfaces, which can help with load transfer and serve as source of sites for both dislocation initiation and annihilation [24]. The strong in-plane strength of graphene can effectively block the movement of dislocations in a matrix and lead to coordinated deformation behavior [25–29]. Therefore, it is reasonable to suppose that the introduction of graphene can improve the mechanical properties by formation of graphene-metal nanolayered
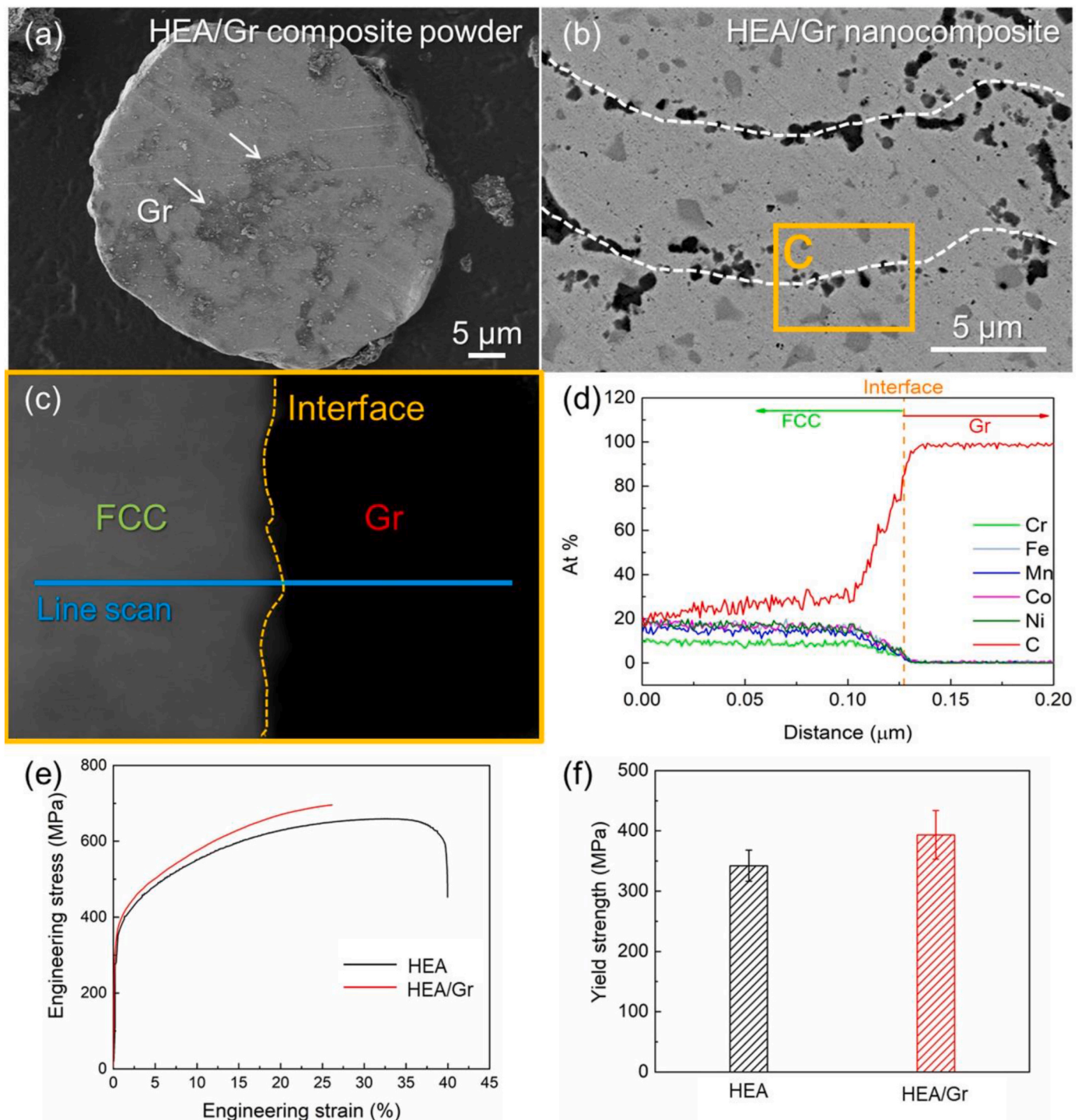

Fig. 1. (a) HEA/Gr composite powder; (b) Microstructure of the HEA/Gr nanocomposite; (c) Interface between HEA and graphene; (d) Element distribution from left to right on line scan; (e) Comparison between HEA and HEA/Gr in stress-strain curve; (f) Comparison in yield strength.

composites. For example, Feng et al. [30] discovered that the greatly increased dislocation density of the composite as compared to that of the pure metal contributed to the strengthening in Al-graphene nano-laminated composites. Inspired by metal/graphene composites, several researchers proposed that adding graphene in HEAs could optimize mechanical properties, as verified experimentally [31–33]. Feng et al. [31] fabricated a nanolayered CoCrFeNi/graphene composite via magnetron sputtering and a transfer process, and revealed that the composites exhibit an ultra-high strength of 4.73 GPa. The micro-strengthening mechanism is revealed as the monolayer graphene

interface effectively being able to block crack propagation and stimulate dislocations to accommodate further deformation. Liu et al. [32] pre-pared laminated CoCrFeMnNi/Graphene bulk material and found a tensile strength of 826.39 MPa. The laminated structure would deflect propagating cracks, and numerous dislocations and twins in the HEA would further increase the strength and plasticity, which was also discovered by Dollmann et al. [34].

Although these experimental studies have demonstrated that gra-phene can play a key role in enhancing strength in HEA, limited by the time and spatial scales of experimental methods, it is challenging to
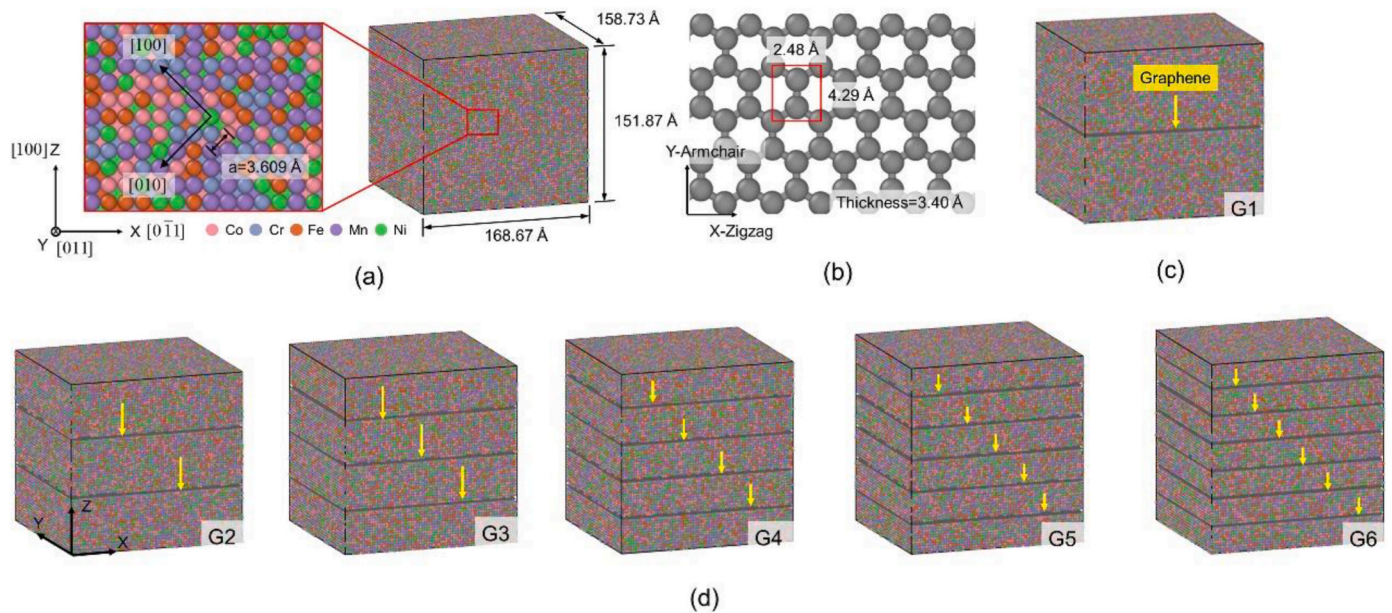
Fig. 2. Atomic schematic diagram: (a) Model of single-crystalline CoCrFeMnNi HEA; (b) Details and parameters of graphene layer; (c) Model of G1; (d) Models with 2–6 layers of graphene, with yellow arrows indicating the position of graphene.

reveal the intrinsic mechanism in graphene-reinforced HEA matrix composites. As a powerful tool to study the deformation and failure mechanisms of materials at the atomic scale, molecular dynamics (MD) simulation has been widely used to explore nanoscale deformation and the interaction mechanism between the plastic carrier and interface in metal-based nanocomposites [35–43] and to study the effect of variables such as temperature or strain rate on the deformation mechanism [44, 45]. For example, Zhang et al. [35] reported a negative Poisson ratio and described the strengthening mechanism in nanolayered graphene/Cu composites. They found that the binding effect of graphene gives the intermediate Cu layer better tensile strength, and the dislocation pile-up observed at the graphene interface provides intuitive evidence for the strengthening mechanism. Liu et al. [36] investigated the mechanism of interfacial strengthening and self-healing effect in graphene/copper nanolayered composites (GCuNL) under shear deformation and discussed factors affecting shear strength. The remarkable self-healing effect in GCuNL composites is realized by interfacial trapping of dislocations. The studies mentioned above do not merely broaden our horizon of strengthening mechanisms in metal/Gr composites at the atomic level, but also manifest that MD simulation is an indispensable method for revealing deformation details and facilitating new structural design.

In light of the above, this work studies the tensile behavior of CoCrFeMnNi HEA/graphene nanocomposites by use of MD simulation, focusing on the effect of the graphene interface on dislocation nucleation and propagation. Further, by adjusting the thickness of the HEA lamellae, we elucidate the size effect of lamellar thickness in the nanocomposites. This work is consistent with our experimental results, which indicates that MD is suitable for exploring the strengthening mechanism of lamellar graphene in HEA composites, and that it can also provide a valuable guideline for the structural design of CoCrFeMnNi HEA/graphene composites.

2. Material and methods

The CoCrFeMnNi HEA/Graphene (HEA/Gr) nanocomposite was synthesized by powder metallurgy [33,46]. As a reference specimen, the CoCrFeMnNi HEA was prepared by the same way. The flaky HEA/Gr powders were examined (Fig. 1(a)) and confirmed that graphene firmly adheres to the flaky HEA powder. Fig. 1(b) shows the microstructure of

the HEA/Gr composites, the 0.5 wt% HEA/Gr composite appeared as a uniform distribution. The graphene sheets were uniformly distributed in the HEA matrix, while graphene and HEA exhibit a layered structure. The interface was characterized via TEM in Fig. 1(c) and the element analysis is shown in Fig. 1(d). Fig. 1(e) shows the tensile properties of the HEA/Gr nanocomposite. The yield strength (Fig. 1(f)) of HEA/Gr (393 MPa) is improved by 15% compared to HEA (342 MPa), which is mainly attributed to the load transform strengthening by the graphene and cooperative plastic deformation due to the superior interface of the HEA and the graphene. Moreover, the graphene hinders dislocation motion. No graphene agglomeration was found, which indicated the uniform dispersion and the excellent interface bonding of HEA/Gr. In order to further explore the details contained in the layered structure and additionally disclose the atomic scale interaction mechanisms between the dislocation and interface, we conducted molecular dynamics simulation to explore the mechanical strengthening mechanism of HEA/Gr composites and provide guidance for their development.

3. Calculation

All simulations in this work are performed using the Large-scale Atomic/Molecular Massively Parallel Simulator (LAMMPS) [47]. The Open Visualization Tool (OVITO) [48] is used for the visualization of the obtained simulation results. The atomistic crystal structure is analyzed via common neighborhood analysis (CNA) [49]. Shear strain is analyzed by atomic strain [50], and the dislocation extraction algorithm (DXA) [51] identifies all dislocation line defects in the crystal.

3.1. Modeling and simulation

The HEA matrix in the experimental HEA/Gr nanocomposite has a complicated polycrystalline structure: several articles have been published on the effect of polycrystallinity on materials. Zhang et al. [52] and Weng et al. [53] studied nanolaminated polycrystalline copper/-graphene. They found that the grain size of copper mainly affects the mechanical behavior in the elastic stage and has a positive effect on the Young's modulus. The dependence of the flow stress on grain size is associated with layer thickness. Zhou et al. [54] investigated nanolaminated polycrystalline aluminum/graphene and observed three forms of dislocation propagation based on aluminum grain size. Besides,

Table 1
Lennard-Jones (LJ) potential parameters for HEA–carbon interactions [66].

Atom-pair	ε (eV)	σ (Å)
Fe–C	0.038687	2.8605
Ni–C	0.038429	2.841
Cr–C	0.037758	2.868
Co–C	0.038281	2.842
Mn–C	0.038021	2.864

the enhancement phase graphene is always non-continuous. Our previous work [55] dealt with the tribological properties of FeNiCrCoCu/non-continuous graphene composites. There, we discussed the effect of graphene size and embedding position on the tribological properties of the material. We found that the graphene interface does not merely cause robust dislocation blockage in the HEA, but also reduces the accumulation of atoms at the surface during sliding. Vardanyan et al. [56] studied Ni/flaked graphene composites via MD and found that differences in the morphology of graphene flakes have various effects on the mechanical properties like the hardness of the composites. Shuang et al. [57,58] systematically studied the interaction between free (non-continuous) and periodic graphene with dislocations and the difference in material strengthening. However, here we intend to focus our problem on a small area near the graphene sheet, so that the graphene may be represented as continuous and the polycrystalline structure as single crystal. We want to highlight the effect of the

dislocation interaction with the interface so that for convenience, we have simplified the experimental model to a single-crystal HEA/-continuous graphene lamellar structure. To build the model of HEA/Gr nanocomposites, an equiatomic single-crystalline CoCrFeMnNi HEA with crystallographic orientations of X-[0$\bar{1}$1], Y-[100] and Z-[011] was first established as shown in Fig. 2(a). The model was constructed by randomly replacing atoms in equal proportion. Considering the compatibility with the size of the graphene lattice, the total dimensions of the HEA crystal in the X, Y, and Z directions are approximately set as 169 Å × 159 Å × 152 Å, producing 348480 atoms. Then a layer of graphene with the same size in the X and Y direction as the HEA model was created as shown in Fig. 2(b), one piece of graphene sheet consists of 10064 atoms, the X-axis being in zigzag direction and Y-axis being armchair. Finally, the HEA/Gr model (G1) was constructed by inserting graphene into the middle of the HEA in X–Y plane, as shown in Fig. 2(c). In an effort to study the change of HEA lamellar thickness on size effect, five models of different graphene content were designed, as shown in Fig. 2(d), which shows the HEA/Gr nanocomposites with 2–6 graphene sheets inserted equidistantly, named G2 … G6 for convenience, respectively.

The entire deformation process can be separated into two steps: equilibrate and tension loading. Periodic boundary conditions are set in X and Y direction, and "shrink-wrapped" conditions are set in Z direction (atoms are not immediately lost should they cross the box boundary). The isobaric-isothermal (NPT) ensemble is used throughout the entire simulation procedure to control the temperature, maintaining a constant
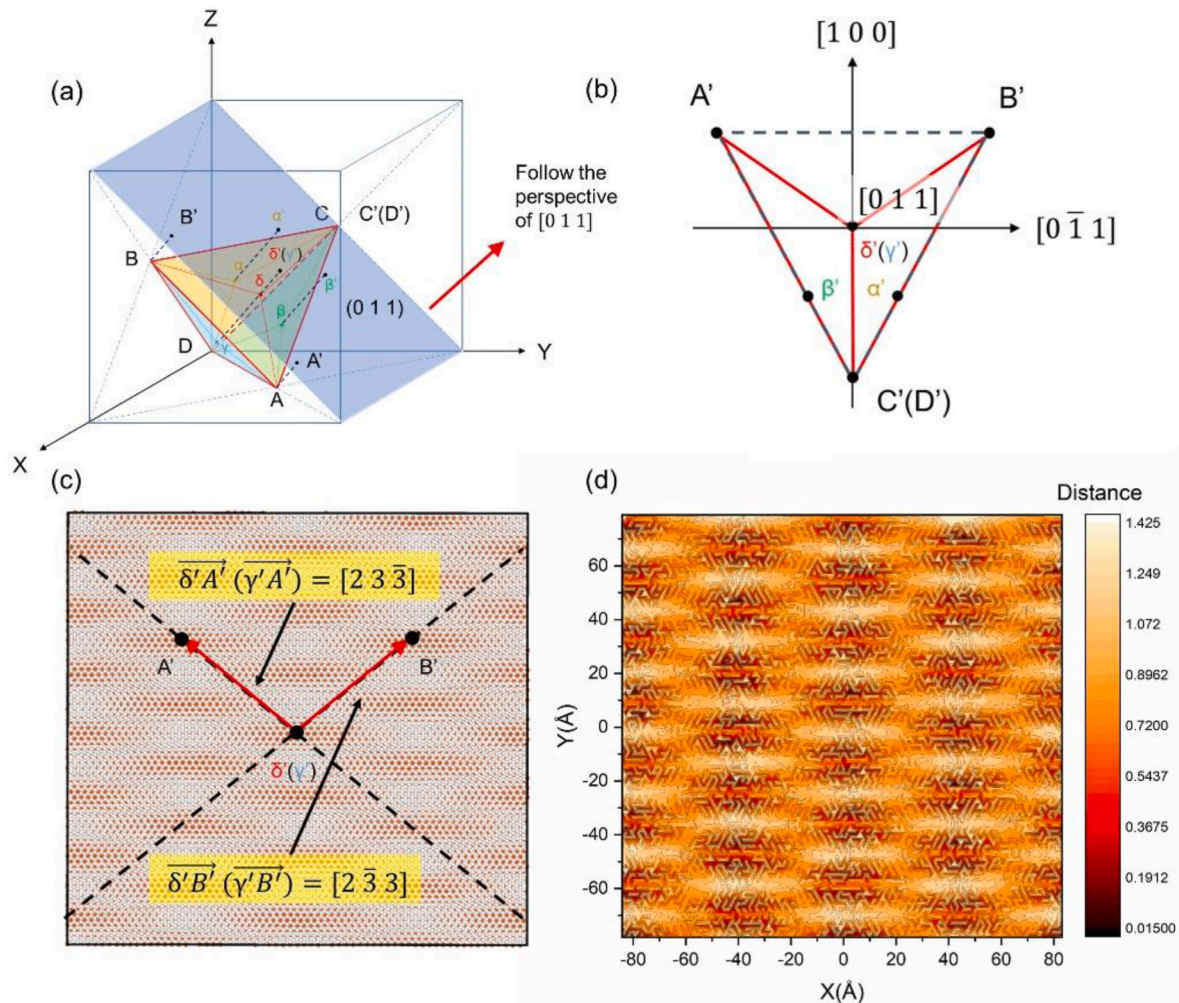
Fig. 3. Moiré pattern and interface dislocation analysis: (a)–(b) The Thompson tetrahedron and its projection onto the [011] plane; (c) Comparison between projected tetrahedron and moiré pattern; (d) Nearest distance between carbon and metal atoms.
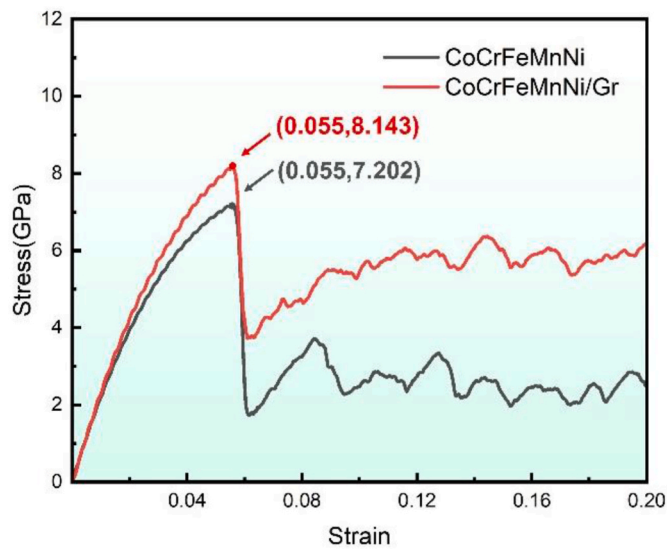
Fig. 4. Stress-strain curves of the pure CoCrFeMnNi and the G1 model.

50 K [59,60] to reduce the impact of temperature disturbances with a Nosé/Hoover thermostat (drag factor 0.2). These composite nano-laminates are initially relaxed for 100 ps to eliminate internal stresses and thus attain the equilibrium state of the models. After relaxation, the

models are stretched uniaxially using the "fix deform" command at an engineering strain rate of $5 \times 10^8\ \mathrm{s^{-1}}$ to a strain of 0.2 along the X or Y directions, respectively [61].

3.2. Interatomic potential

The interactions among HEA atoms are described by a table spline potential [62], which is a recently developed, appropriate, and tested pair potential for CoCrFeMnNi HEA [63]. The adaptive intermolecular reactive empirical bond order (AIREBO) potential [64] is confirmed as a common and reliable potential to describe the interactions of carbon atoms, consequently AIREBO with a Lennard-Jones cutoff scale factor of 3.0 (corresponding to 10.2 Å in real units) is used to represent the co-valent bonds of the carbon atoms of each individual graphene layer. The interactions between HEA atoms and carbon atoms are described by the Lennard-Jones (LJ) potential [65]. A multitude of studies have suc-cessfully proved that the LJ potential can describe the complex situation in metal/graphene composites [35–37]. The used LJ parameters are shown in Table .1.

4. Results and discussion

4.1. Structure and mechanical properties of HEA/Gr nanocomposites

4.1.1. Interface structure
It is indispensable to analyze the specific interface structures because of the lattice mismatch and atomic stacking between the CoCrFeMnNi
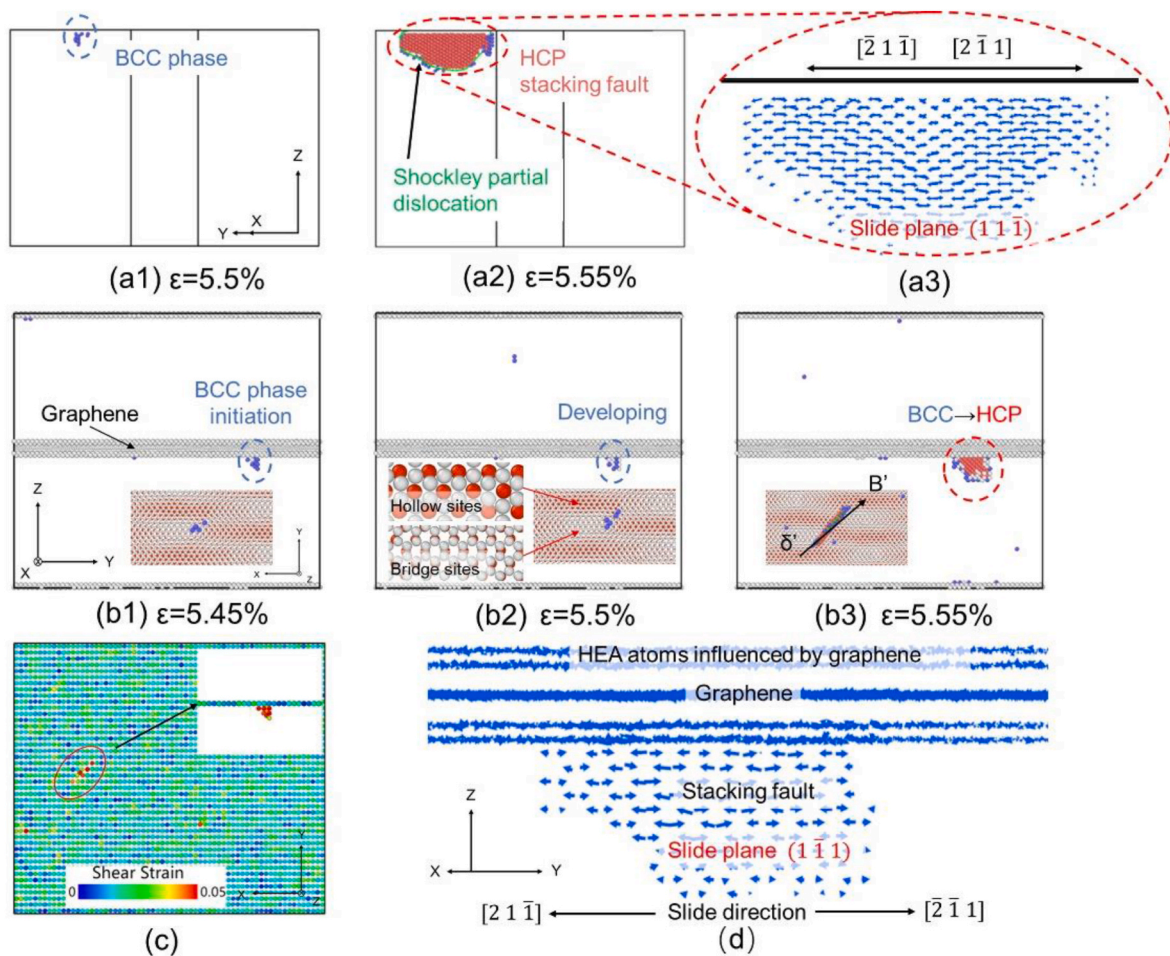
Fig. 5. Details of the heterogeneous nucleation of dislocations: (a1)-(a3) Dislocation nucleation in pure CoCrFeMnNi; (b1) -(b3) Dislocation nucleation in the G1 model, white atoms in the inset represent carbon, red ones represent metal; (c) Shear strain in interface atoms; (d) Atom displacement in the interface of the G1 model.
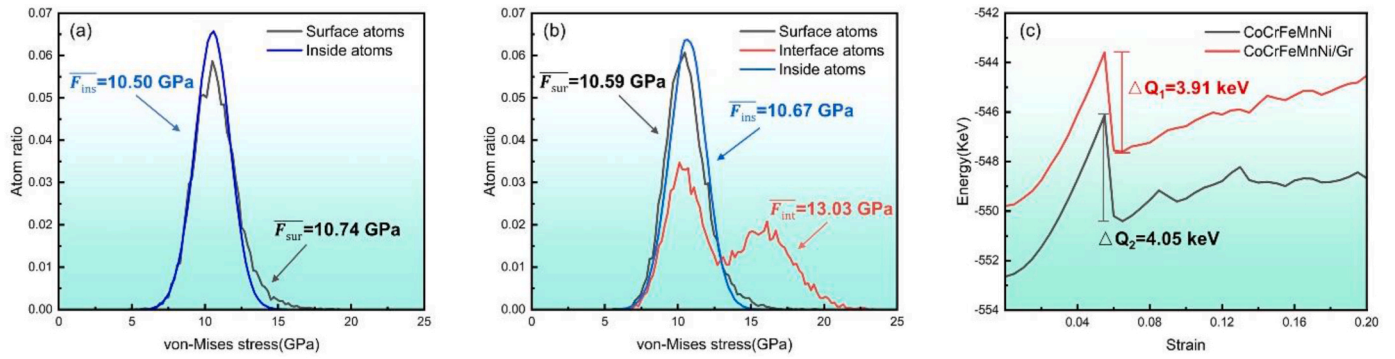
Fig. 6. (a) Von-Mises stress in pure HEA; (b) Von-Mises stress in the G1 model; (c) Comparison of activation free energy between HEA and HEA/Gr.

matrix and the graphene layers before the investigation of mechanical properties and deformation details. Since graphene and the HEA matrix both have a periodic and regular crystallographic structure, the HEA/Gr interface forms periodic moiré patterns. Besides, due to the rather large lattice mismatch between graphene and the HEA matrix, one is likely to find misfit dislocations in the interface [67]. Peng et al. compared moiré patterns at graphene/metal interface with Thompson tetrahedra to obtain the Burgers vector of interfacial dislocation [68]. In this work, the Burgers vector of misfit dislocation cannot be readily characterized directly compared with Thompson tetrahedra, since the stacking index of the HEA/Gr interface is [011]. Extending from Wang's work [69], a Thompson tetrahedron is projected onto the [011] plane (Fig. 3(a)), and the plane projection is shown in Fig. 3(b). By contrasting the projection with the moiré pattern at the interface (Fig. 3(c)), it can be found that the vector directions of the interface dislocations are $\overrightarrow{\delta'A'} = [23\overline{3}]$ and $\overrightarrow{\delta'B'} = [2\overline{3}3]$. These interface dislocations have an effect on lattice dislocation nucleation in the tensile process, which will be described later on. Fig. 3(d) used misfit interval statistical method (MISM) [70] to identify the geometrical characteristics of a moiré pattern. As shown in Fig. 3(d), each carbon atom in the graphene has the nearest metal atom in the HEA matrix. Their in-plane (xy plane) distance is defined as the misfit Δl_{ij} for each atom. It can be calculated as [70]:

$$\Delta l_{ij} = \min\left\{ P \middle| P = \sqrt{(x_i - x_j)^2 + (y_i - y_j)^2}, j \in N \right\} (i \in M) \quad (1)$$

where x and y are the coordinates of carbon atoms i and HEA atoms j, N and M are the total numbers of atoms in the carbon and HEA layers, respectively. Fig. 3(d) explains the origin of red and white area in Fig. 3(c).

4.1.2. Stress-strain curves

Fig. 4 shows the stress-strain curves of the pure CoCrFeMnNi and the G1 models under uniaxial tensile load along the X-axis. The trends of the two curves exhibit some similarities: both curves can be divided into the elastic deformation stage and the plastic deformation stage. In the elastic stage, the stress increases approximately linearly with the increase of strain to the maximum (yield strength). After yielding, the stress drops significantly, then fluctuates within a relatively balanced range. Compared with the pure CoCrFeMnNi model, the yield strain barely changes after the addition of a single layer of graphene, and the yield strength and elastic modulus improve by 13% and 16%, respectively. Moreover, the flow stress in the plastic deformation stage increases substantially by 90%. It can also be observed that the introduction of graphene significantly reduces the fluctuation of the flow stress [71]. In Figs. S1 and S2 in the Supplementary Information, we briefly explore the effects of different strain rates and deformation temperatures on tensile test results. Moreover, in Fig. S3 in the Supplementary Information we elucidate the effect of (non-)continuity of the embedded graphene nanosheets on the HEA/graphene stress-strain curves.

4.2. Deformation mechanism of HEA/Gr nanocomposites

4.2.1. Inhomogeneous nucleation of dislocations

Fig. 5(a1) and (a2) indicate the dislocation nucleation in CoCr-FeMnNi. It can be seen that the dislocation nucleates on the free surface in the positive Z-direction, this is due to the relatively high von-Mises stress at the free surface (Fig. 6(a)). Before the formation of dislocations, BCC clusters agglomerate, and these clusters transform into dislocation nuclei and continue to expand into HCP structural stacking faults with applied strain [72]. Fig. 5(a3) shows the atomic displacement in the stacking fault formed by the motion of a Shockley partial dislocation, and the result shows that the dislocation slips along the $(11\overline{1})$ plane towards $[\overline{2}1\overline{1}]$ and $[2\overline{1}1]$.

Fig. 5(b1)-(b3) show the initial dislocation nucleation in HEA/Gr nanocomposites. We observed that the dislocation nucleation site is not on the free surface, but on the HEA/Gr interface. Like pure HEAs, dislocation nucleation also goes through the process from FCC to BCC clusters and then to HCP stacking faults (SFs). The insets clearly display the relationship between nucleation position and the moiré pattern at the interface. A BCC cluster appears between the hollow site and bridge site, which is the specific structure that the HEA/Gr interface forms. The interface section of the SF is coincident with the interface dislocation $\overrightarrow{\delta'B'}$, which is reliable evidence that the lattice dislocation nucleation is driven by the interface dislocation [73]. Fig. 5(c) presents the shear strain for the inset in Fig. 5(b1), which indicates that the BCC cluster forms at the location with the maximum shear strain. Atomic displacement details of the SF are shown in Fig. 5(d). The binding and limiting effect that the graphene layer imposes on the two adjacent atomic layers of the HEA matrix can be clearly visualized, which corroborates the coordination deformation behavior. Thus, the initial SF occurs below the third layer of atoms and slip along the $(1\overline{1}1)$ plane towards direction of $[21\overline{1}]$ and $[21\overline{1}]$, which is consistent with Schmid's theory discussed in 4.3.2.

Fig. 6 analyzes the alteration of the total von-Mises stress and free energy of the system before and after inserting graphene. Comparing Fig. 6(a) and (b), the addition of the graphene sheet slightly decreases the stress of the surface atoms and increases the stress of the inside atoms. Importantly, the addition creates two interface layers with larger stress, which reflects the load transfer effect. This much more easily satisfies the stress conditions for dislocation nucleation, and thus leads to greater probability of nucleation in the HEA/Gr interface. The nucleation rate can be expressed using the Arrhenius equation [74]:

$$\nu = N\nu_0 \exp\left(-\frac{Q(\sigma, T)}{\kappa_B T} \right) \quad (2)$$

Here, ν_0 is the attempt frequency, N is the number of nucleation sites, and Q is the activation free energy. Obviously, when other variables remain unchanged, the nucleation rate ν decreases monotonically as Q increases. Fig. 6(c) suggests that the pure HEA has more activation free
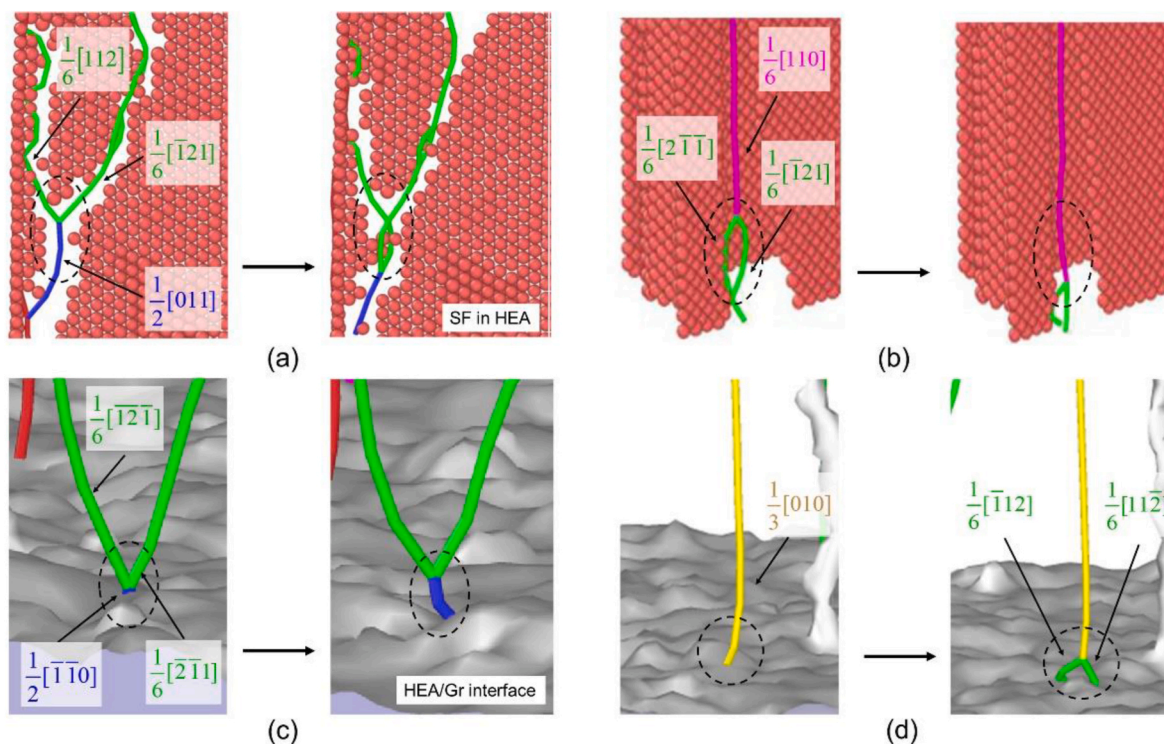
Fig. 7. Dislocation reactions in materials: (a) Perfect dislocation decomposition; (b) Stair-rod dislocation composition; (c) Perfect dislocation composition in the interface; (d) Hirth dislocation decomposition in the interface. Specific dislocation types and corresponding colors are listed in title of Fig. 10.

energy than the HEA/Gr nanocomposites, so the HEA/Gr interface is more conducive to dislocation nucleation.

4.2.2. Dislocation reactions

Generally, Shockley partial dislocations easily collide with each other and react to generate immovable dislocations such as stair-rod and Hirth dislocations in FCC metals, because plastic deformation is mediated by a large number of partial dislocation slips. The reason why they are called immovable dislocations is that they are located on the {110} and {100} planes, respectively, and have a certain angle with the {111} planes, so they are not easily moved on a large scale during deformation. Fig. 7(a) and (b) show the typical dislocation reaction including perfect dislocation decomposition and stair-rod dislocation composition inside the CoCrFeMnNi HEA matrix. The reaction equation is as follows:

$$\frac{1}{2}[011] \rightarrow \frac{1}{6}[112] + \frac{1}{6}[\bar{1}21] \tag{3}$$

$$\frac{1}{6}[2\bar{1}\bar{1}] + \frac{1}{6}[\bar{1}21] \rightarrow \frac{1}{6}[110] \tag{4}$$

These two equations describe classical dislocation decomposition in an FCC crystal. Arrows from left to right reflect a decrease in energy, thus are spontaneous.

In the HEA/Gr nanocomposites, the above dislocation reaction is still the main mechanism in the matrix. The effect of graphene on dislocation propagation has been discussed in many studies [58,75–77]. Kim et al. [75] pointed out that the unique two-dimensional network of graphene and strong C–C covalent bond can effectively constrain dislocation motion. Li et al. [77] also found that graphene at the grain boundaries of
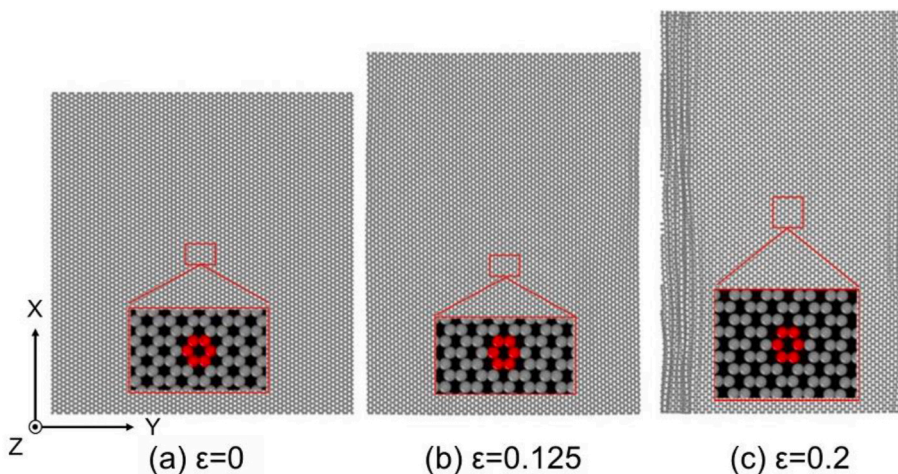
Fig. 8. In-plane deformation of graphene. With increasing strain, the hexagonal structure elongates in the direction of tension (X), and wrinkles parallel to the direction of tension form on the graphene sheet (see the sides of panel c).
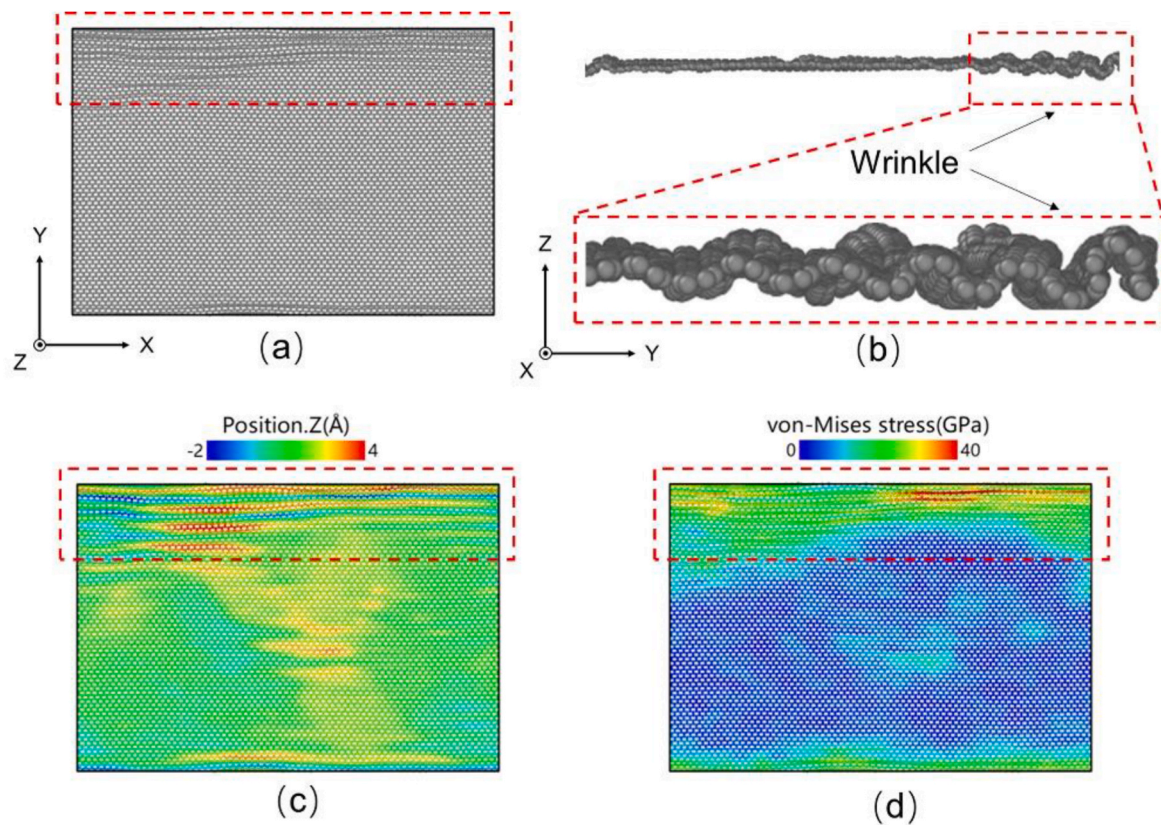
Fig. 9. Graphene wrinkle analysis (ε = 0.185): (a)–(b) Geometrical wrinkle appearance; (c) Degree of out-of-plane wrinkle deflection; (d) Von-Mises stress in graphene sheet.

nanostructured metals would enhance the strong dislocation hindrance. This effect makes the dislocation lines in the HEA lamella short and dense, and affects the work hardening in the plastic stage. Fig. 7(c) and (d) show the role of graphene in the dislocation reaction. As shown in Fig. 7(c), where two Shockley partial dislocations on the same plane approach, they are blocked by the graphene sheet and react with each other to generate a perfect dislocation. This reaction is the reverse reaction of Eq. (3) and requires energy absorption. Fig. 7(d) describes the
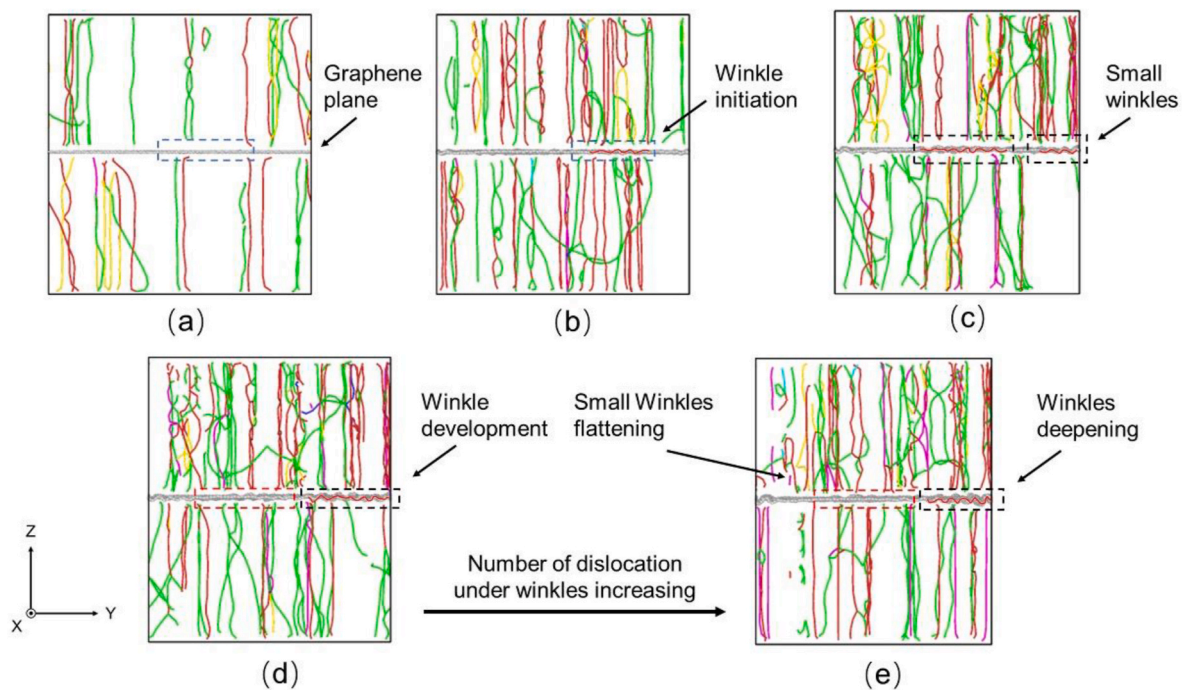
Fig. 10. The deformation process of graphene. (Yellow: Hirth dislocation; green: Shockley partial dislocation; pink: stair-rod dislocation; deep blue: perfect dislocation; light blue: Frank dislocation; red: other dislocation).
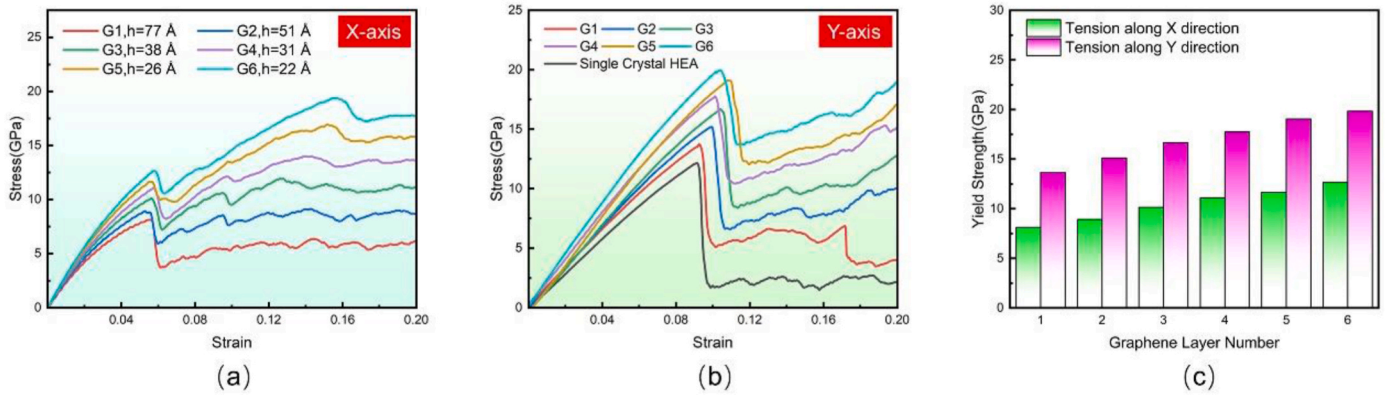
Fig. 11. Stress-strain curves for HEA and HEA/Gr nanocomposites (G1–G6): (a) Tension along X-axis; (b) Tension along Y-axis; (c) Yield strength comparison.

decomposition process of a Hirth dislocation into two partial dislocations, which is also a reverse reaction process requiring energy absorption. Such reactions have been observed at the HEA/Gr interface via MD [78], which indicates that the interface can provide energy for dislocation composition or decomposition.

4.2.3. Deformation of graphene

The in-plane deformation of graphene is shown in Fig. 8. The initial structure of graphene is a perfect hexagon composed of carbon atoms (Fig. 8(a)). Under tension, the lattice elongates along the tension direction (X-direction), contracts along the Y-direction, and gradually changes into a deformed hexagonal structure, as shown in the inset of Fig. 8(b) and (c). It is worth noting that "wrinkles" are generated on the graphene sheet parallel to the direction of tension, visible on both sides of the simulation box in Fig. 8(c). When the strain reaches 0.185, these wrinkles become more obvious. Fig. 9(a) and (b) illustrate the wrinkles' appearance along the X direction. In Fig. 9(c), we colored the C atoms according to the local wrinkle height in Z direction, the out-of-plane deflection range is approximately -2 to 4 Å, greater than the thickness of graphene. Fig. 9(d) shows the distribution of the von-Mises stress in the graphene sheet, where it can be seen that the stresses in the wrinkle are much higher than in the flat part of the sheet.

To explore the causes of the wrinkles, we further track the out-of-plane deformation process of graphene. In the initial plastic deformation stage, dislocations occur and propagate in the metal matrix, while the graphene remains flat (Fig. 10(a)). The wrinkles first occur, accompanied by dislocations, when the strain reaches 12.5% (Fig. 10 (b)). Via comparison of the blue boxes in Fig. 10(a) and (b), it can be seen that the movement of dislocations towards the graphene interface leads to the formation of wrinkles. By the time the strain has reached 16%, many dispersive small wrinkles have been generated in the graphene sheet (black boxes in Fig. 10(c)). As the strain continues to increase, several small wrinkles flatten (red box in Fig. 10(d)), while others exhibit an increased degree of folding (black box in Fig. 10(d)). A comparison between the black boxes in Fig. 10(d) and (e) suggests that when the wrinkles surpass a certain amplitude, they can also become a dislocation source to emit dislocations, which is in line with the research of Xie et al. [78].

4.3. Size effect

4.3.1. Effect of HEA lamella thickness and tensile direction

Fig. 11(a) and (b) show the stress-strain curves of G1 – G7 tension along the X and Y directions, respectively. The statistical yield strength is shown in Fig. 11(c). In the same tensile direction, the yield strength increases significantly with an increase in the number of graphene layers. By comparing the models with the same number of graphene layers, it can be seen that the yield strength can be improved by

Table 2
Schmid factors for tension in X and Y direction (the maximum values of each column are marked bold).

Slip plane	FCC slip systems	Tension direction X-$[0\bar{1}1]$	Tension direction Y-$[100]$
$(\bar{1}\bar{1}1)_\alpha$	$[\bar{1}\bar{1}2]$	0.236	0.236
	$[2\bar{1}1]$	**0.471**	**0.471**
	$[\bar{1}21]$	0.236	0.236
$(1\bar{1}\bar{1})_\gamma$	$[2\bar{1}1]$	0	**0.471**
	$[1\bar{1}2]$	0	0.236
	$[12\bar{1}]$	0	0.236
$(\bar{1}1\bar{1})_\beta$	$[\bar{1}2\bar{1}]$	0.236	0.236
	$[\bar{1}12]$	0.236	0.236
	$[21\bar{1}]$	**0.471**	**0.471**
$(111)_\delta$	$[1\bar{2}1]$	0	0.236
	$[\bar{2}11]$	0	**0.471**
	$[11\bar{2}]$	0	0.236

stretching along Y direction. There are two main reasons for this phenomenon: the graphene orientation and the anisotropy of the FCC matrix. The tensile strength along the armchair direction of graphene is better than that along the zigzag direction [79]. Fig. 2(b) showed that the X-direction is the zigzag direction, and the Y-direction is the armchair direction. Moreover, several groups have studied the influence of crystal orientation on the deformation mechanism and mechanical properties. From an energetic point of view, the tensile yield strength along the [100] direction is greater than that along the $[0\bar{1}1]$ direction for FCC crystals [80,81]. This is because the activation volume of dislocation nucleation is smaller and the nucleation energy barrier is larger in the [100] direction than in the $[0\bar{1}1]$ direction, so more stress is required to nucleate under tension along the [100] direction [82]. Zhang et al. [83] investigated the deformation behavior of CoCrFeNi HEA single-crystalline micro/nanopillars with different orientations. They revealed that deformation twinning is a dominant deformation mechanism in [100] oriented micro/nanopillars, while the nucleation and slip of full dislocations dominate plastic deformation in both [110] and [111] oriented micro/nanopillars, which agrees well with our own simulations.

4.3.2. Schmid factor controlled slip process

The Schmid factor is the ratio of resolved shear stress to axial stress, which generally corresponds to the difficulty of starting the slip system. It is calculated as [84]:

$$m = \cos \varphi \cos \lambda \tag{5}$$

where φ represents the angle between the normal direction of the slip plane and the tension direction, λ represents the angle between the
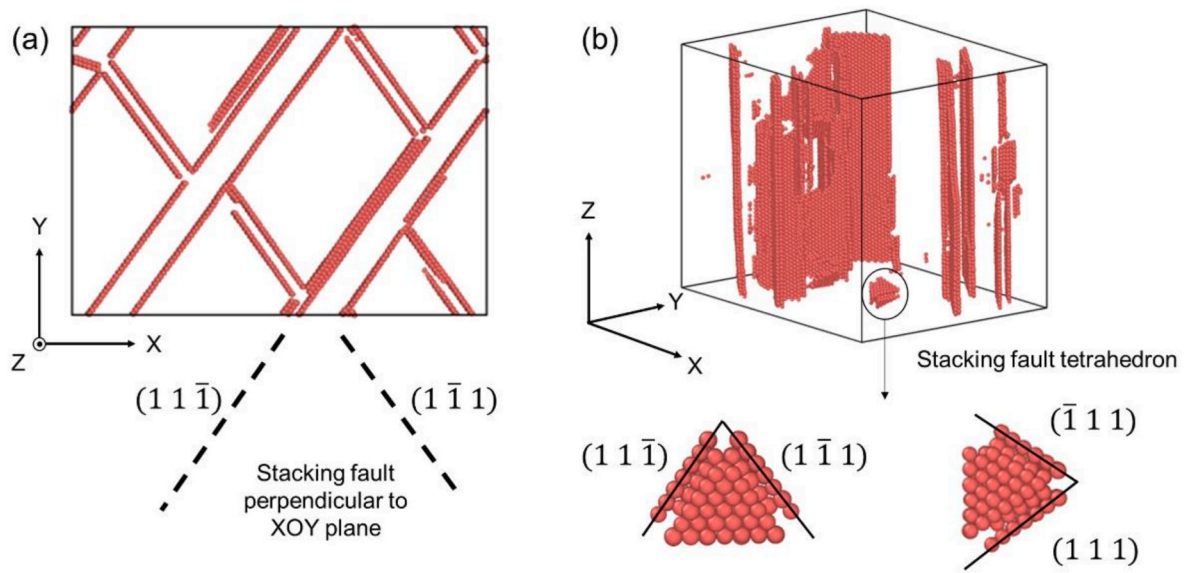
Fig. 12. Stacking fault morphology: (a) Tension along X-axis; (b) Tension along Y-axis.
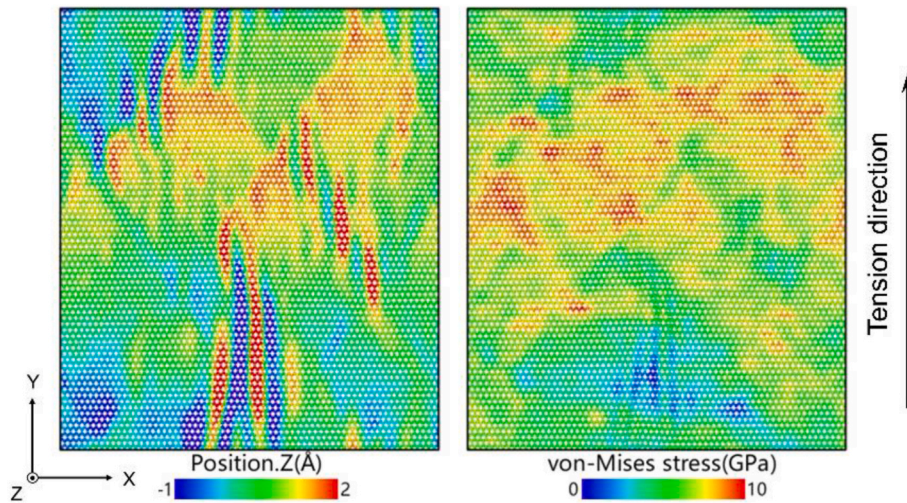
Fig. 13. Wrinkle of G1 model with tension along the Y-axis: (a) Out-of-plane height of wrinkle; (b) Von-Mises stress of the graphene sheet.

sliding direction and the tension direction [85]. In the pure CoCrFeMnNi single crystal, the Schmid factors for tension along X-$[0\bar{1}1]$ and Y-$[100]$ are summarized in Table 2. According to the data in the table, when stretching along X-direction, two slip systems $(\bar{1}\bar{1}1)_\alpha[2\bar{1}1]$ and $(\bar{1}1\bar{1})_\beta$ $[21\bar{1}]$ are activated first. The initial slip plane and slip direction shown in Fig. 5(a3) and (d) are consistent with the calculated result. Then dislocations slide in accordance with the $(\bar{1}\bar{1}1)$ and the $(\bar{1}1\bar{1})$ slip planes, producing cross-type stacking faults in the X–Y plane as shown in Fig. 12 (a). When tension acts along the Y direction, dislocations can move along four slip planes, so a stacking fault tetrahedron can be formed as shown in Fig. 12(b). Besides, because the dislocation motion is not completely perpendicular to the X–Y plane while tension acts along the Y-direction, the stress concentration is not obvious, resulting in the relative dispersion of the wrinkles in the graphene sheet, as shown in Fig. 13.

4.3.3. Hall-Petch effect in HEA/Gr nanocomposites

In Fig. 11, it can be seen that the strength of the nanocomposites changes with the layer thickness. In particular, a quantitative relationship between the yield strength and the thickness of the HEA lamellae is

established. In polycrystalline materials, the Hall-Petch effect is used to describe the relationship between grain size and yield strength [86]. The equation is as follows:

$$\sigma_s = \sigma_0 + \frac{k}{\sqrt{d}} \tag{6}$$

where σ_s is the yield strength, d is the grain size, k and σ_0 are material parameters. This equation is an empirical model for the law of fine grain strengthening, which has good applicability to all kinds of materials, including HEA [17,87,88]. Recently, the application of the Hall-Petch effect has been extended to nanocomposites to describe the relationship between strength and layer thickness [89]. However, Eq. (6) only allows a single variable, but in this paper, there are two variables: the thickness of the HEA lamella t_{HEA} and the thickness of the graphene layer t_{Gr}. These two unequal thickness values cannot be substituted into Eq. (6) at the same time, so they need to be converted into an equivalent thickness t [90].

Taking the G2 model as an example, the idea of an equivalent transformation of layers with unequal thickness is introduced. As shown in Fig. 14(a), the original model on the left side is composed of three
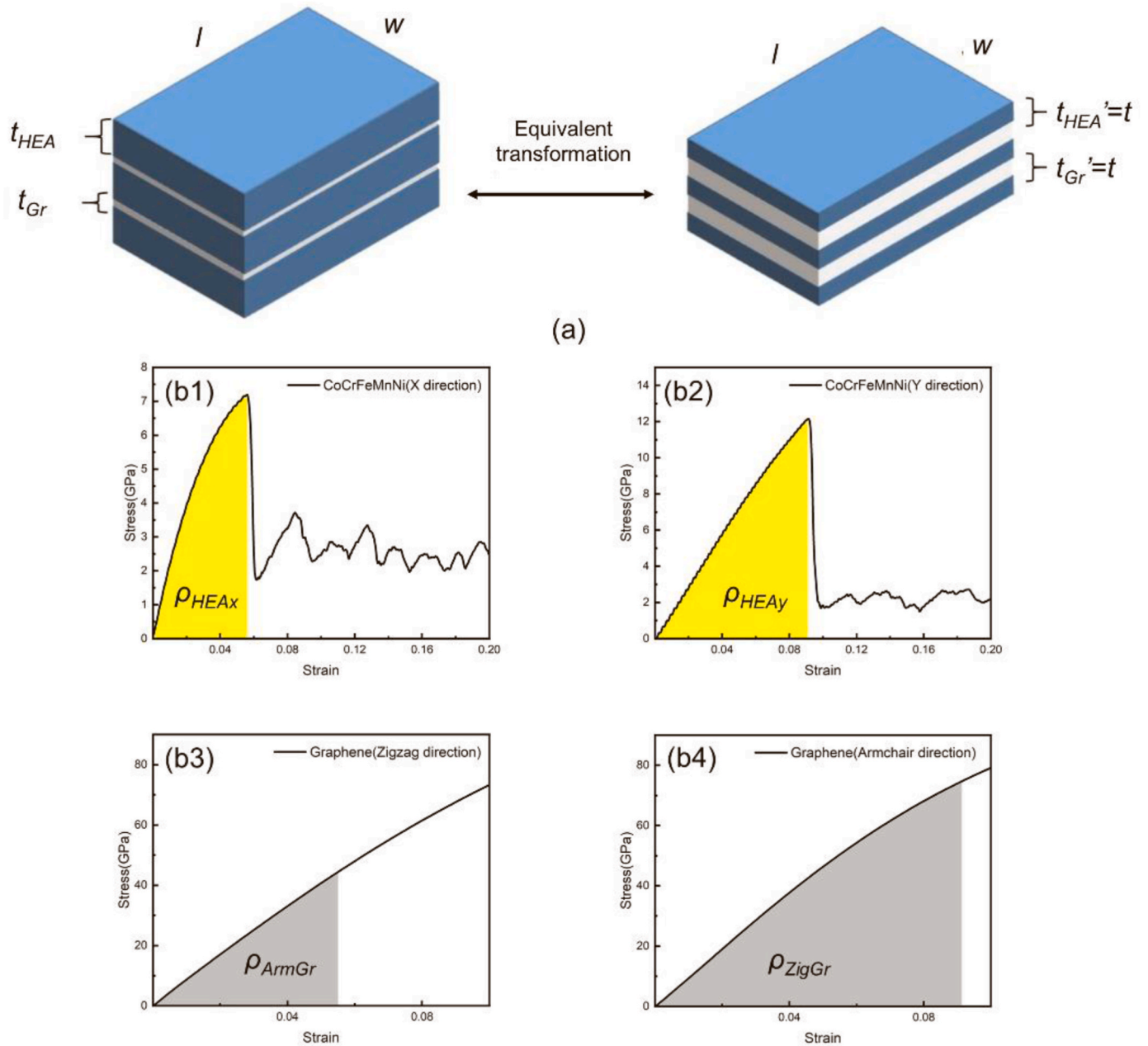
Fig. 14. Theory of equivalent transformation: (a) Diagram of the transformation; (b1) -(b4) Integral calculation of elastic strain energy.

layers of HEA (blue) and two layers of graphene (white), in which l and w represent the length and width of the model, while t_{HEA} and t_{Gr} represent the thickness of one layer of HEA and graphene, respectively. The model on the right side is the equivalent model, and the thickness of HEA and graphene can be normalized to the equivalent thickness t. The transformation of the two models is based on the conservation of strain energy in the elastic stage of materials, which writes as follows [90]:

$$\Phi = \Phi_{HEA} + \Phi_{Gr} = \Phi'_{HEA} + \Phi'_{Gr} \tag{7}$$

here, Φ is the total strain energy, Φ_{HEA}, Φ'_{HEA}, Φ_{Gr}, and Φ'_{Gr} represent the strain energies of HEA and graphene before and after the conversion, respectively. Assuming that x layers of graphene are inserted into $(x+1)$ HEA layers, the following formula can be obtained:

$$\Phi_{HEA} = (x+1)\rho_{HEA}V_{HEA} = (x+1)\rho_{HEA}t_{HEA}lw \tag{8}$$

$$\Phi_{Gr} = x\rho_{Gr}V_{Gr} = x\rho_{Gr}t_{Gr}lw \tag{9}$$

here, V_{HEA} and V_{Gr} are the volumes of the CoCrFeMnNi lamella and graphene, ρ_{HEA} and ρ_{Gr} represent the corresponding strain energies per unit volume, which can be calculated as the integral of the area under the stress-strain curves from zero to the yield strain, shown as a yellow area in Fig. 14(b1) -(b4). The strain energy per unit volume is multiplied by the volume to obtain the overall strain energy. Assuming that the equivalent thickness of the HEA lamella and the graphene layer is t after the equivalent transformation, as follows:

$$\Phi'_{HEA} = (x+1)\rho_{HEA}V_{HEA} = (x+1)\rho_{HEA}tlw \tag{10}$$

$$\Phi'_{Gr} = x\rho_{Gr}V_{Gr} = x\rho_{Gr}tlw \tag{11}$$

The expression of the equivalent thickness t can be obtained by combining the above formulas:

$$t = \frac{(x+1)\rho_{HEA}t_{HEA} + x\rho_{Gr}t_{Gr}}{(x+1)\rho_{HEA} + x\rho_{Gr}} \tag{12}$$

$$\sigma_s = 2.578 + \frac{25.354}{\sqrt{t}}$$

$$\sigma_s = 3.315 + \frac{37.926}{\sqrt{t}}$$
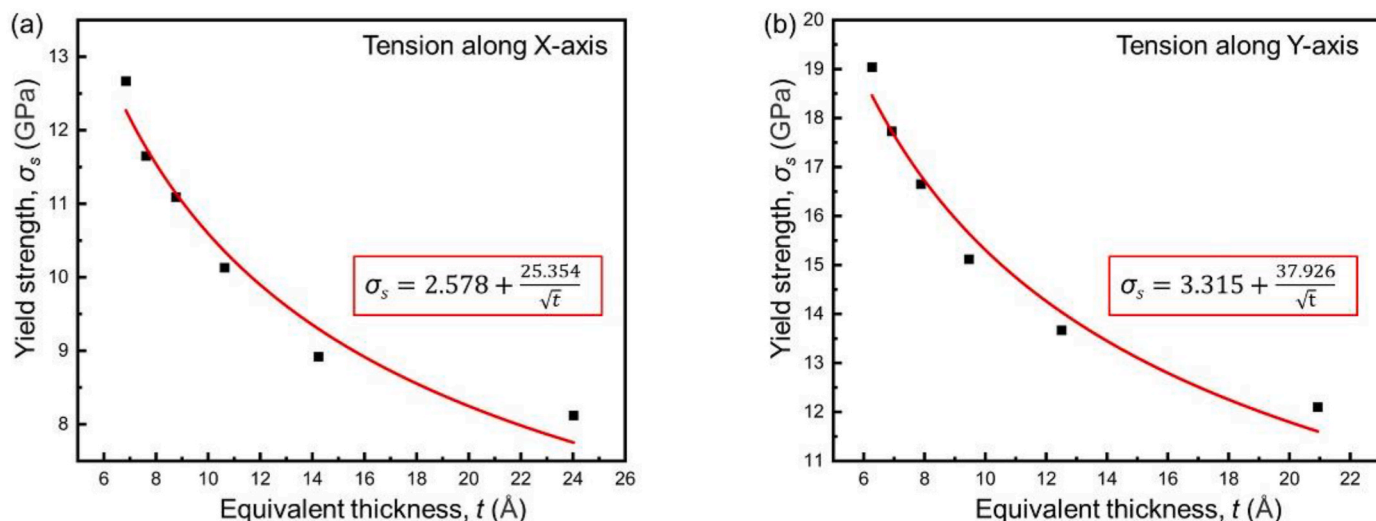
Fig. 15. Hall-Petch relationship fitting for the results of two tension directions: (a) Tension in X-axis; (b) Tension in Y-axis. Note the different scaling, especially of the ordinate axes.

By substituting the known quantity, the equivalent thickness t corresponding to the thickness of each HEA lamella can be obtained. With t as the abscissa and the corresponding yield strength as the ordinate, the Hall- Petch relationship curve can be fitted as shown in Fig. 15. By comparing the relationship between scatter points and fitting curve, it is found that the maximum error is less than 5%, which suggests that the fitting is reasonable. Therefore, the Hall-Petch relationship can better describe the influence of the thickness of the HEA lamella on the yield strength of the composites. Hou et al. [91] used MD simulations to find that with the reduction of CoCrFeMnNi grain size (from 3.6 Å to 2.0 Å), small grains will cause the entire material to be amorphous, resulting in softening, which causes the yield strength of the material to exhibit inverse Hall-Petch behavior. Jiang et al. [92,93] found that in nanocrystalline high-entropy alloys, the microscopic deformation mechanism of the Hall-Petch relation is that the accumulation of dislocations at the grain boundaries leads to an increase in the strength of HEA. Inverse Hall-Petch behavior, on the other hand, is caused by the migration of grain boundaries and the rotation and merging of grains, a conclusion to which Chen et al. [94] came as well. In our study, even if the lamellar thickness of the HEA reaches 20–30 Å, it still exhibits reliable Hall-Petch-type behavior, which strongly illustrates the superiority and predictability of the graphene interface in strengthening the tensile properties of HEAs.

5. Conclusions

This study employed molecular dynamics (MD) simulations to elucidate and augment the understanding of the tensile characteristics of CoCrFeMnNi high-entropy alloy/graphene nanocomposites. The MD simulation can provide guidance for the structural design of composite materials. The principal findings can be summarized as follows:

(1) Experimental evidence indicates that the CoCrFeMnNi high-entropy alloy/graphene nanocomposite, characterized by a layered structure, exhibits superior mechanical properties compared to its monolithic counterpart.
(2) Atomistic analysis reveals that the HEA/Gr interface exhibits a clear moiré pattern, and the vector directions of interfacial dislocations are $[23\bar{3}]$ and $[2\bar{3}3]$, which has a bearing on the dislocation nucleation of the composites.
(3) The introduction of the graphene interface can act as a source for heterogeneous nucleation of dislocations. The interface does not only impede dislocation propagation, but also furnishes energy

for dislocation reactions. Under tensile loading, graphene undergoes "wrinkling" due to stress concentration resulting from dislocation activity.
(4) Reorienting the tensile direction from the X-axis to the Y-axis has a beneficial effect on the mechanical characteristics and induces a change in the slip system. Moreover, a reduction in the equivalent layer thickness, as determined by an equivalence model, leads to an increase in the yield stress of the HEA/Gr nanolaminate, which conforms to the Hall-Petch relationship.

Credit author statement

Yeran Shi: Methodology, Software, Validation, Formal analysis, Investigation, Data curation, Writing – original draft. **Wenting Ye**: Experiment, Data curation, Investigation, Writing – original draft. **Dongpeng Hua**: Methodology, Validation, Formal analysis. **Zhuobin Huang**: Investigation, Formal analysis, Data curation. **Yuxin Liu**: Investigation, Formal analysis, Data curation. **Qing Zhou**: Conceptualization, Writing – review & editing, Supervision, Funding acquisition. **Shuo Li**: Investigation, Data curation. **Ting Guo**: Investigation, Data curation. **Yongnan Chen**: Conceptualization, Investigation, Data curation. **Stefan J. Eder**: Data curation, Writing – review & editing, Funding acquisition. **Haifeng Wang**: Writing – review & editing, Supervision, Funding acquisition.

Declaration of competing interest

The authors declare that they have no known competing financial interests or personal relationships that could have appeared to influence the work reported in this paper.

Data availability

Data will be made available on request.

Austrian COMET-Program (Project K2 InTribology1, no. 872176) and carried out at the Austrian Excellence Center for Tribology (AC2T research GmbH). Open access funding provided by TU Wien (TUW).

Appendix A. Supplementary data

Supplementary data to this article can be found online at https://doi.org/10.1016/j.mtphys.2023.101220.

References

[1] Q.Q. Ding, Y. Zhang, X. Chen, X.Q. Fu, D.K. Chen, S.J. Chen, L. Gu, F. Wei, H.B. Bei, Y.F. Gao, M.R. Wen, J.X. Li, Z. Zhang, T. Zhu, R.O. Ritchie, Q. Yu, Tuning element distribution, structure and properties by composition in high-entropy alloys, Nature 574 (7777) (2019) 223–+.

[2] E.P. George, W.A. Curtin, C.C. Tasan, High entropy alloys: a focused review of mechanical properties and deformation mechanisms, Acta Mater. 188 (2020) 435–474.

[3] Z.Z. Li, S.T. Zhao, R.O. Ritchie, M.A. Meyers, Mechanical properties of high-entropy alloys with emphasis on face-centered cubic alloys, Prog. Mater. Sci. 102 (2019) 296–345.

[4] E.P. George, D. Raabe, R.O. Ritchie, High-entropy alloys, Nat. Rev. Mater. 4 (8) (2019) 515–534.

[5] L. Wang, F. Zhang, Z. Nie, L. Wang, F. Wang, B. Wang, S. Zhou, Y. Xue, B. Cheng, H. Lou, X. Chen, Y. Ren, D.E. Brown, V. Prakapenka, E. Greenberg, Z. Zeng, Q. S. Zeng, Abundant polymorphic transitions in the Al0.6CoCrFeNi high-entropy alloy, Mater. Today Phys. 8 (2019) 1–9.

[6] Y.F. Ye, Q. Wang, J. Lu, C.T. Liu, Y. Yang, High-entropy alloy: challenges and prospects, Mater. Today 19 (6) (2016) 349–362.

[7] Y. Ren, Z. Huang, Y. Wang, Q. Zhou, T. Yang, Q. Li, Q. Jia, H. Wang, Friction-induced rapid amorphization in a wear-resistant (CoCrNi)88Mo12 dual-phase medium-entropy alloy at cryogenic temperature, Compos. B Eng. 263 (2023): 110833.

[8] B. Cantor, Multicomponent high-entropy Cantor alloys, Prog. Mater. Sci. 120 (2021).

[9] B. Gludovatz, A. Hohenwarter, D. Catoor, E.H. Chang, E.P. George, R.O. Ritchie, A fracture-resistant high-entropy alloy for cryogenic applications, Science 345 (6201) (2014) 1153–1158.

[10] A.Y. Gerard, J. Han, S.J. McDonnell, K. Ogle, E.J. Kautz, D.K. Schreiber, P. Lu, J. E. Saal, G.S. Frankel, J.R. Scully, Aqueous passivation of multi-principal element alloy Ni38Fe20Cr22Mn10Ca10: unexpected high Cr enrichment within the passive film, Acta Mater. 198 (2020) 121–133.

[11] S.J. Sun, Y.Z. Tian, X.H. An, H.R. Lin, J.W. Wang, Z.F. Zhang, Ultrahigh cryogenic strength and exceptional ductility in ultrafine-grained CoCrFeMnNi high-entropy alloy with fully recrystallized structure, Mater.Today Nano 4 (2018) 46–53.

[12] M.J. Yao, K.G. Pradeep, C.C. Tasan, D. Raabe, A novel, single phase, non-equiatomic FeMnNiCoCr high-entropy alloy with exceptional phase stability and tensile ductility, Scripta Mater. 72–73 (2014) 5–8.

[13] G. Laplanche, A. Kostka, O.M. Horst, G. Eggeler, E.P. George, Microstructure evolution and critical stress for twinning in the CrMnFeCoNi high-entropy alloy, Acta Mater. 118 (2016) 152–163.

[14] F. Otto, A. Dlouhy, C. Somsen, H. Bei, G. Eggeler, E.P. George, The influences of temperature and microstructure on the tensile properties of a CoCrFeMnNi high-entropy alloy, Acta Mater. 61 (15) (2013) 5743–5755.

[15] S.J. Sun, Y.Z. Tian, H.R. Lin, X.G. Dong, Y.H. Wang, Z.J. Zhang, Z.F. Zhang, Enhanced strength and ductility of bulk CoCrFeMnNi high entropy alloy having fully recrystallized ultrafine-grained structure, Mater. Des. 133 (2017) 122–127.

[16] Y. Han, H.B. Li, H. Feng, K.M. Li, Y.Z. Tian, Z.H. Jiang, Enhancing the strength and ductility of CoCrFeMnNi high-entropy alloy by nitrogen addition, Mater.Sci. Eng. A-Struct. Mater. Prop. Microst. Process. vol. 789 (2020).

[17] J.H. Zhang, R.D. Fu, Y.J. Li, Y. Lei, L. Guo, H.Y. Lv, J.X. Yang, Synergistic enhancement in strength and ductility of nitrogen-alloyed CoCrFeMnNi high-entropy alloy via multi-pass friction stir processing, J. Alloys Compd. 927 (2022).

[18] S. Son, J. Lee, P. Asghari-Rad, G.H. Gu, F. Haftlang, H.S. Kim, A facile strengthening method by co-doping boron and nitrogen in CoCrFeMnNi high-entropy alloy, Mater. Sci. Eng. Struct. Mater. Prop. Microst. Process. 846 (2022).

[19] K.S. Novoselov, A.K. Geim, S.V. Morozov, D. Jiang, Y. Zhang, S.V. Dubonos, I. V. Grigorieva, A.A. Firsov, Electric field effect in atomically thin carbon films, Science 306 (5696) (2004) 666–669.

[20] X.-K. Kong, C.-L. Chen, Q.-W. Chen, Doped graphene for metal-free catalysis, Chem. Soc. Rev. 43 (8) (2014) 2841–2857.

[21] X. Li, J.G. Yu, S. Wageh, A.A. Al-Ghamdi, J. Xie, Graphene in photocatalysis: a review, Small 12 (48) (2016) 6640–6696.

[22] S. Stankovich, D.A. Dikin, G.H.B. Dommett, K.M. Kohlhaas, E.J. Zimney, E. A. Stach, R.D. Piner, S.T. Nguyen, R.S. Ruoff, Graphene-based composite materials, Nature 442 (7100) (2006) 282–286.

[23] C. Lee, X.D. Wei, J.W. Kysar, J. Hone, Measurement of the elastic properties and intrinsic strength of monolayer graphene, Science 321 (5887) (2008) 385–388.

[24] M. Yang, Y. Liu, T.X. Fan, D. Zhang, Metal-graphene interfaces in epitaxial and bulk systems: a review, Prog. Mater. Sci. 110 (2020).

[25] S. Dixit, A. Mahata, D.R. Mahapatra, S.V. Kailas, K. Chattopadhyaya, Multi-layer graphene reinforced aluminum - manufacturing of high strength composite by friction stir alloying, Compos. B Eng. 136 (2018) 63–71.

[26] X. Huang, X.Y. Qi, F. Boey, H. Zhang, Graphene-based composites, Chem. Soc. Rev. 41 (2) (2012) 666–686.

[27] B.Y. Ju, Z.H. Yu, H.S. Gou, W.S. Yang, G.Q. Chen, G.H. Wu, Coordinated matrix deformation induced ductility in multilayer graphene/aluminum composites, Carbon 202 (2023) 31–40.

[28] J.C. Li, X.X. Zhang, L. Geng, Effect of heat treatment on interfacial bonding and strengthening efficiency of graphene in GNP/Al composites, Compos. Appl. Sci. Manuf. 121 (2019) 487–498.

[29] V. Singh, D. Joung, L. Zhai, S. Das, S.I. Khondaker, S. Seal, Graphene based materials: past, present and future, Prog. Mater. Sci. 56 (8) (2011) 1178–1271.

[30] S.W. Feng, Q. Guo, Z. Li, G.L. Fan, Z.Q. Li, D.B. Xiong, Y.S. Su, Z.Q. Tan, J. Zhang, D. Zhang, Strengthening and toughening mechanisms in graphene-Al nanolaminated composite micro-pillars, Acta Mater. 125 (2017) 98–108.

[31] X.B. Feng, K. Cao, X.G. Huang, G.D. Li, Y. Lu, Nanolayered CoCrFeNi/graphene composites with high strength and crack resistance, Nanomaterials 12 (12) (2022).

[32] C.Y. Liu, X.S. Jiang, H.L. Sun, Y.L. Zhang, Y.J. Fang, R. Shu, Microstructure and mechanical properties of bioinspired laminated CoCrFeNiMn high entropy alloy matrix composites reinforced with graphene, Mater. Sci. Eng. Struct. Mater. Prop. Microst. Process. 859 (2022).

[33] W.T. Ye, M.D. Xie, Z.B. Huang, H.M. Wang, Q. Zhou, L. Wang, B. Chen, H.F. Wang, W.M. Liu, Microstructure and tribological properties of in-situ carbide/CoCrFeNiMn high entropy alloy composites synthesized by flake powder metallurgy, Tribol. Int. 181 (2023).

[34] A. Dollmann, A. Kauffmann, M. Heilmaier, A.S. Tirunilai, L.S. Mantha, C. Kubel, S. J. Eder, J. Schneider, C. Greiner, Dislocation-mediated and twinning-induced plasticity of CoCrFeMnNi in varying tribological loading scenarios, J. Mater. Sci. 57 (36) (2022) 17448–17461.

[35] C. Zhang, C. Lu, L.Q. Pei, J.Q. Li, R. Wang, K. Tieu, The negative Poisson's ratio and strengthening mechanism of nanolayered graphene/Cu composites, Carbon 143 (2019) 125–137.

[36] X.Y. Liu, F.C. Wang, W.Q. Wang, H.A. Wu, Interfacial strengthening and self-healing effect in graphene-copper nanolayered composites under shear deformation, Carbon 107 (2016) 680–688.

[37] D.P. Hua, Q. Zhou, W. Wang, S. Li, X.R. Liu, H.F. Wang, Atomic mechanism on the mechanical and tribological performance of amorphous/graphene nanolaminates, Tribol. Int. 165 (2022).

[38] Q. Jia, W.H. He, D.P. Hua, Q. Zhou, Y. Du, Y. Ren, Z.B. Lu, H.F. Wang, F. Zhou, J. Wang, Effects of structure relaxation and surface oxidation on nanoscopic wear behaviors of metallic glass, Acta Mater. 232 (2022).

[39] W. Wang, D. Hua, Q. Zhou, S. Li, S.J. Eder, J. Shi, Z. Wang, H. Wang, W. Liu, Effect of a water film on the material removal behavior of Invar during chemical mechanical polishing, Appl. Surf. Sci. 616 (2023): 156490.

[40] L.R. Safina, K.A. Krylova, J.A. Baimova, Molecular dynamics study of the mechanical properties and deformation behavior of graphene/metal composites, Mater. Today Phys. 28 (2022).

[41] K.K. Qiu, X.D. Wang, T.D. Xu, Q.P. Cao, S.Q. Ding, D.X. Zhang, K.A. Beyer, J. Z. Jiang, Two-step annealing induced structural rejuvenation: a cause for memory effect in metallic glasses, Mater. Today Phys. 27 (2022).

[42] I. Szlufarska, Atomistic simulations of nanoindentation, Mater. Today 9 (5) (2006) 42–50.

[43] W. Wang, D.P. Hua, D.W. Luo, Q. Zhou, S. Li, J.Q. Shi, H.F. Wang, Molecular dynamics simulation of deformation mechanism of CoCrNi medium entropy alloy during nanoscratching, Comput. Mater. Sci. 203 (2022).

[44] J. Jiang, P.W. Chen, J.L. Qiu, W.F. Sun, I. Saikov, V. Shcherbakov, M. Alymov, Microstructural evolution and mechanical properties of AlxCoCrFeNi high-entropy alloys under uniaxial tension: a molecular dynamics simulations study, Mater. Today Commun. 28 (2021).

[45] L.L. Wang, W.T. Liu, B.Y. Zhu, W. Chen, F. Zhang, B. Liu, J.L. Liu, J.Q. Zhou, Y. H. Zhao, Influences of strain rate, Al concentration and grain heterogeneity on mechanical behavior of CoNiFeAlxCu1-x high-entropy alloys: a molecular dynamics simulation, J. Mater. Res. Technol. Jmr&T 14 (2021) 2071–2084.

[46] N. Guo, B.F. Luan, F.F. He, Z.Q. Li, Q. Liu, Influence of flake thickness on the shape and distribution of Al2O3 particles in Al matrix composites fabricated by flake powder metallurgy, Scripta Mater. 78–79 (2014) 1–4.

[47] A.P. Thompson, H.M. Aktulga, R. Berger, D.S. Bolintineanu, W.M. Brown, P. S. Crozier, P.J. in 't Veld, A. Kohlmeyer, S.G. Moore, T.D. Nguyen, R. Shan, M. J. Stevens, J. Tranchida, C. Trott, S.J. Plimpton, Lammps - a flexible simulation tool for particle-based materials modeling at the atomic, meso, and continuum scales, Comput. Phys. Commun. 271 (2022): 108171.

[48] A. Stukowski, Visualization and analysis of atomistic simulation data with OVITO-the Open Visualization Tool, Model. Simulat. Mater. Sci. Eng. 18 (1) (2010).

[49] J.D. Honeycutt, H.C. Andersen, Molecular-dynamics study of melting and freezing of small Lennard-Jones clusters, J. Phys. Chem. 91 (19) (1987) 4950–4963.

[50] F. Shimizu, S. Ogata, J. Li, Theory of shear banding in metallic glasses and molecular dynamics calculations, Mater. Trans. 48 (11) (2007) 2923–2927.

[51] A. Stukowski, V.V. Bulatov, A. Arsenlis, Automated identification and indexing of dislocations in crystal interfaces, Model. Simulat. Mater. Sci. Eng. 20 (8) (2012).

[52] M.R. Zhang, T. Fu, Z.Y. Fang, S.Y. Weng, X.H. Peng, Feature size coupling effect of nanolaminated graphene/copper composites, Int. J. Mech. Sci. 227 (2022).

[53] S.Y. Weng, Z.Y. Fang, Y.B. Zhao, T. Fu, X.H. Peng, Molecular dynamics studies on size effects in laminated polycrystalline graphene/copper composites: implications for mechanical behavior, ACS Appl. Nano Mater. 4 (11) (2021) 12289–12299.

[54] X.H. Zhou, X. Liu, J.J. Shang, Q.S. Yang, Grain-size effect on plastic flow stress of nanolaminated polycrystalline aluminum/graphene composites, Mech. Mater. 148 (2020).

[55] S. Li, W.T. Ye, Y.R. Shi, Q. Zhou, Y.N. Chen, T. Guo, Y.X. Liu, L.C. Zhang, H. F. Wang, Atomistic simulation and experimental verification of tribological behavior of high entropy alloy/graphene composite coatings, Surf. Coating. Technol. 467 (2023).

[56] V.H. Vardanyan, H.M. Urbassek, Morphology of graphene flakes in Ni-graphene nanocomposites and its influence on hardness: an atomistic study, Carbon 185 (2021) 660–668.

[57] F. Shuang, K.E. Aifantis, Dislocation-graphene interactions in Cu/graphene composites and the effect of boundary conditions: a molecular dynamics study, Carbon 172 (2021) 50–70.

[58] F. Shuang, Z.H. Dai, K.E. Aifantis, Strengthening in metal/graphene composites: capturing the transition from interface to precipitate hardening, ACS Appl. Mater. Interfaces 13 (22) (2021) 26610–26620.

[59] Z.D. Sha, P.S. Branicio, H.P. Lee, T.E. Tay, Strong and ductile nanolaminate composites combining metallic glasses and nanoglasses, Int. J. Plast. 90 (2017) 231–241.

[60] D.P. Hua, W.T. Ye, Q. Jia, Q. Zhou, Q.S. Xia, J.Q. Shi, Y.Y. Deng, H.F. Wang, Molecular dynamics simulation of nanoindentation on amorphous/amorphous nanolaminates, Appl. Surf. Sci. 511 (2020).

[61] Y.M. Qi, M. Zhao, M.L. Feng, Molecular simulation of microstructure evolution and plastic deformation of nanocrystalline CoCrFeMnNi high-entropy alloy under tension and compression, J. Alloys Compd. 851 (2021).

[62] R. Groger, V. Vitek, A. Dlouhy, Effective pair potential for random fcc CoCrFeMnNi alloys, Model. Simulat. Mater. Sci. Eng. 28 (7) (2020).

[63] M. Heczko, V. Mazanova, R. Groger, T. Zalezak, M.S. Hooshmand, E.P. George, M. J. Mills, A. Dlouhy, Elemental segregation to lattice defects in the CrMnFeCoNi high-entropy alloy during high temperature exposures, Acta Mater. 208 (2021).

[64] T. Belytschko, S.P. Xiao, G.C. Schatz, R.S. Ruoff, Atomistic simulations of nanotube fracture, Phys. Rev. B 65 (23) (2002).

[65] S.P. Huang, D.S. Mainardi, P.B. Balbuena, Structure and dynamics of graphite-supported bimetallic nanoclusters, Surf. Sci. 545 (3) (2003) 163–179.

[66] Y.Q. Tang, D.Y. Li, Nano-tribological behavior of high-entropy alloys CrMnFeCoNi and CrFeCoNi under different conditions: a molecular dynamics study, Wear 476 (2021).

[67] A.G. Sheinerman, Plastic deformation and fracture processes in metal/graphene composites: a review, Crit. Rev. Solid State Mater. Sci. 47 (5) (2022) 708–735.

[68] W.X. Peng, K. Sun, Interface structures and dislocation nucleation of Cu/graphene interface via molecular dynamic simulations, Materialia 18 (2021).

[69] C.J. Wang, Z.R. Liu, B.N. Yao, X.F. Kong, D. Legut, R.F. Zhang, Y. Deng, Effects of hydrogen clusters on interface facilitated plasticity at semi-coherent bimetal interfaces, Scripta Mater. 190 (2021) 63–68.

[70] H.Z. Bai, H.W. Bao, Y. Li, H.D. Xu, S.Z. Li, F. Ma, Moire pattern based universal rules governing interfacial superlubricity: a case of graphene, Carbon 191 (2022) 28–35.

[71] Q. Zhou, D.W. Luo, D.P. Hua, W.T. Ye, S. Li, Q.G. Zou, Z.Q. Chen, H.F. Wang, Design and characterization of metallic glass/graphene multilayer with excellent nanowear properties, Friction 10 (11) (2022) 1913–1926.

[72] D.P. Hua, Q.S. Xia, W. Wang, Q. Zhou, S. Li, D. Qian, J.Q. Shi, H.F. Wang, Atomistic insights into the deformation mechanism of a CoCrNi medium entropy alloy under nanoindentation, Int. J. Plast. 142 (2021).

[73] I.J. Beyerlein, J. Wang, R.F. Zhang, Mapping dislocation nucleation behavior from bimetal interfaces, Acta Mater. 61 (19) (2013) 7488–7499.

[74] A.S. Khan, J. Liu, A deformation mechanism based crystal plasticity model of ultrafine-grained/nanocrystalline FCC polycrystals, Int. J. Plast. 86 (2016) 56–69.

[75] Y. Kim, J. Lee, M.S. Yeom, J.W. Shin, H. Kim, Y. Cui, J.W. Kysar, J. Hone, Y. Jung, S. Jeon, S.M. Han, Strengthening effect of single-atomic-layer graphene in metal-graphene nanolayered composites, Nat. Commun. 4 (2013).

[76] Z.L. Qiu, Z.B. Zhang, Y.N. Xiong, X. Luo, Z.Q. Li, K.H. Zheng, W.Y. Hu, Size effects of graphene sheets on the strengthening mechanism of Al-graphene composites: a molecular dynamics study, Appl. Surf. Sci. 596 (2022).

[77] Z. Li, H.T. Wang, Q. Guo, Z.C. Li, D.B. Xiong, Y.S. Su, H.J. Gao, X.Y. Li, D. Zhang, Regain strain-hardening in high-strength metals by nanofiller incorporation at grain boundaries, Nano Lett. 18 (10) (2018) 6255–6264.

[78] H.C. Xie, Z.C. Ma, W. Zhang, H.W. Zhao, L.Q. Ren, Strengthening effect of high-entropy alloys endowed by monolayer graphene, Mater. Today Phys. 27 (2022).

[79] H. Zhao, K. Min, N.R. Aluru, Size and chirality dependent elastic properties of graphene nanoribbons under uniaxial tension, Nano Lett. 9 (8) (2009) 3012–3015.

[80] Y.J. Gao, H.B. Wang, J.W. Zhao, C.Q. Sun, F.Y. Wang, Anisotropic and temperature effects on mechanical properties of copper nanowires under tensile loading, Comput. Mater. Sci. 50 (10) (2011) 3032–3037.

[81] Y. Wen, W. Yunxin, Effects of temperature and pressure on elastic properties of single crystal aluminum in different crystal orientations, Phys. Status Solidi B 257 (12) (2020).

[82] M.A. Tschopp, D.L. McDowell, Influence of single crystal orientation on homogeneous dislocation nucleation under uniaxial loading, J. Mech. Phys. Solid. 56 (5) (2008) 1806–1830.

[83] Q. Zhang, R.R. Huang, J.X. Jiang, T.Q. Cao, Y.P. Zeng, J.G. Li, Y.F. Xue, X.Y. Li, Size effects and plastic deformation mechanisms in single-crystalline CoCrFeNi micro/nanopillars, J. Mech. Phys. Solid. 162 (2022).

[84] Q. Liu, D.J. Jensen, N. Hansen, Effect of grain orientation on deformation structure in cold-rolled polycrystalline aluminium, Acta Mater. 46 (16) (1998) 5819–5838.

[85] J. Song, D.J. Srolovitz, Atomistic simulation of multicycle asperity contact, Acta Mater. 55 (14) (2007) 4759–4768.

[86] N. Hansen, Hall-Petch relation and boundary strengthening, Scripta Mater. 51 (8) (2004) 801–806.

[87] B. Gwalani, V. Soni, M. Lee, S.A. Mantri, Y. Ren, R. Banerjee, Optimizing the coupled effects of Hall-Petch and precipitation strengthening in a Al0.3CoCrFeNi high entropy alloy, Mater. Des. 121 (2017) 254–260.

[88] S. Yoshida, T. Ikeuchi, T. Bhattacharjee, Y. Bai, A. Shibata, N. Tsuji, Effect of elemental combination on friction stress and Hall-Petch relationship in face-centered cubic high/medium entropy alloys, Acta Mater. 171 (2019) 201–215.

[89] X.L. Zhou, C.Q. Chen, Strengthening and toughening mechanisms of amorphous/amorphous nanolaminates, Int. J. Plast. 80 (2016) 75–85.

[90] Z.C. Xie, W.R. Jian, Z.H. Wang, X.Q. Zhang, X.H. Yao, Layer thickness effects on the strengthening and toughening mechanisms in metallic glass-graphene nanolaminates, Comput. Mater. Sci. 177 (2020).

[91] J.L. Hou, Q. Li, C.B. Wu, L.M. Zheng, Atomic simulations of grain structures and deformation behaviors in nanocrystalline CoCrFeNiMn high-entropy alloy, Materials 12 (7) (2019).

[92] J. Jiang, W.F. Sun, N. Luo, P.W. Chen, Atomic-scale analysis of deformation behavior of face-centered cubic nanocrystalline high-entropy alloys with different grain sizes at high strain rates, Mater. Chem. Phys. 300 (2023).

[93] J. Jiang, W.F. Sun, N. Luo, Atomic insights into effects of temperature and grain diameter on the micro-deformation mechanism, mechanical properties and sluggish diffusion of nanocrystalline high-entropy alloys, Mater. Today Commun. 33 (2022).

[94] S. Chen, Z.H. Aitken, Z.X. Wu, Z.G. Yu, R. Banerjee, Y.W. Zhang, Hall-Petch and inverse Hall-Petch relations in high-entropy CoNiFeAlxCu1-x alloys, Mater. Sci. Eng. Struct. Mater. Prop. Microst. Process. 773 (2020).